Space Weather

RESEARCH ARTICLE
10.1029/2021SW002878

Key Points:

- High spatiotemporal resolution 3-D structures of daytime E_s over Japan are reconstructed from ground-based Global Navigation Satellite System total electron content
- Time-dependent empirical orthogonal functions based on ionosonde observations are used to vertically constrain the E region solution
- For the first time, computerized ionospheric tomography with ground-based GNSS TEC is shown to reproduce the E_s-layer altitude time variation

Supporting Information:

Supporting Information may be found in the online version of this article.

Correspondence to:
W. Fu,
fu.weizheng.40y@st.kyoto-u.ac.jp

Citation:

Fu, W., Ssessanga, N., Yokoyama, T., & Yamamoto, M. (2021). High-resolution 3-D imaging of daytime sporadic-E over Japan by using GNSS TEC and ionosondes. *Space Weather*, *19*, e2021SW002878. https://doi.org/10.1029/2021SW002878

Received 13 AUG 2021
Accepted 3 DEC 2021

Author Contributions:

Conceptualization: Weizheng Fu, Nicholas Ssessanga, Tatsuhiro Yokoyama
Formal analysis: Weizheng Fu
Methodology: Weizheng Fu, Nicholas Ssessanga
Project Administration: Mamoru Yamamoto
Software: Weizheng Fu
Supervision: Tatsuhiro Yokoyama, Mamoru Yamamoto

High-Resolution 3-D Imaging of Daytime Sporadic-E Over Japan by Using GNSS TEC and Ionosondes

Weizheng Fu[1], **Nicholas Ssessanga**[1,2], **Tatsuhiro Yokoyama**[1], **and Mamoru Yamamoto**[1]

[1]Research Institute for Sustainable Humanosphere, Kyoto University, Uji, Japan, [2]Department of Physics, 4DSpace, University of Oslo, Oslo, Norway

Abstract

A novel two-step three-dimensional (3-D) computerized ionospheric tomography (CIT) technique has been developed to image the structure of daytime midlatitude sporadic-E (E_s). The CIT relies on total electron content (TEC) from a dense ground-based Global Navigation Satellite System (GNSS) receiver network over the Japan area. First, on a coarse grid, the TEC data and a multiplicative algebraic reconstruction technique (MART) are used to reconstruct the F region from a smooth background. Then, on a fine grid and using singular value decomposition (SVD), the residues after deducting the F region contribution to TEC are utilized in reconstructing the E region, extending 80–180 km in altitude. To vertically constrain the E region solution, we introduced a family of subsets of time-dependent empirical orthogonal functions (EOFs) from a Chapman model function tuned to manually scaled ionosonde observations. We analyzed three event days to validate the results. East-West (E-W) aligned frontal structures, spanning several hundred kilometers, migrating northward in the morning and southward in the afternoon, were observed. The new technique effectively tracks the E_s-height variation over time, which had proved difficult to reproduce in earlier tempts at 3-D E_s reconstructions.

Plain Language Summary

Sporadic-E, abbreviated as E_s, are small-scale plasma irregularities that occur in altitudes between 95 and 120 km. The patchy nature of E_s causes radio wave amplitude and phase scintillations, which deters navigation and communication system that operate in the frequency range below a few GHz. To date, the generation mechanism of E_s is not yet fully understood, partly due to the lack of coherent, consistent, and continuous broad three-dimensional (3-D) plasma density distribution measurements on E_s scale size. This paper presents a novel computerized ionospheric tomography technique to reconstruct the 3-D structure of daytime midlatitude E_s with a high spatiotemporal resolution. The tomography technique relies on a network of ground-based ionosondes and Global Navigation Satellite System (GNSS) receivers over Japan. Results show that reconstructed 2-D horizontal slices of E_s agree with earlier findings on E_s morphology and dynamics. More importantly, for the first time, we can track the E_s-layer altitude-time variation.

1. Introduction

Sporadic-E (E_s) are electron density inhomogeneities manifested in the ionospheric E region. At midlatitude area, during the daytime, E_s is suggested to occur due to reinforced metallic (of meteoric origin) ionization in altitude range ~95–120 km (Whitehead, 1989). Occasionally, E_s becomes denser than the normal E- and F-layer densities, exhibiting a high correlation of occurrence with intense transionospheric signal scintillation (Maeda & Heki, 2014). Consequently, to forecast and draw patterns in the scintillation morphology, the space weather community has extensively investigated the E_s structure both theoretically and experimentally. For example, information on the horizontal structures of midlatitude E_s has been inferred by using ionosondes (Whitehead, 1972), radars (Miller & Smith, 1975), and rockets (Yamamoto et al., 1998). More so, S. Saito et al. (2006) obtained three-dimensional (3-D) structures of E_s patches by using the middle and upper atmosphere (MU) radar at Shigaraki, Japan. Wu et al. (2005) deduced occurrence rates and intensities of E_s at summertime midlatitudes, by using radio occultation measurements around the globe. Haldoupis (2011) and references therein have discussed an excellent tutorial review that summarizes the results from most of these studies and their affirmation on the E_s structure. The literature suggests that the occurrence of E_s varies with local time, altitude, latitude, longitude, and seasons, and its existence depends on the tidal wind, the Earth's geomagnetic field, and the level of meteoric depositions (Whitehead, 1989). Even with such rich literature, the E_s generating mechanisms are not fully understood, although the wind shear theory driven by zonal winds has widely been accepted for the E_s occurrence in the midlatitudes (Andoh et al., 2020, 2021; Maeda et al., 2016; Shinagawa et al., 2017; Tsunoda

Validation: Weizheng Fu, Nicholas Ssessanga
Writing – original draft: Weizheng Fu
Writing – review & editing: Nicholas Ssessanga, Tatsuhiro Yokoyama

et al., 2004; Yokoyama et al., 2005, 2009). A major challenge in ascertaining such E_s mechanisms has for long been the lack of observation techniques with sufficient spatial-temporal (4-D) coverage to fully track the trajectory and distribution of plasma densities during the formation and occurrence of E_s. Fortunately, the advent and advances of GNSS (Global Navigation Satellite System) technology have offered cost-effective ways of probing the ionosphere at a broader horizontal scale and higher temporal resolution. At midlatitudes, specifically over Japan, Maeda and Heki (2014, 2015) have used ground-based observations from a dense GNSS receivers network to reconstruct clear 2-D structures of daytime E_s. In their results, the frontal horizontal structure of E_s was oriented in the East-West (E-W) direction, spanning over ∼100 km and migrating with speeds of 30–100 m/s. Albeit inferences from such 2-D analyses are encouraging, the missing height dimension poses limitations on the information that can be inferred.

In this paper, we present a novel two-stage 3-D computerized ionospheric tomography (CIT) technique based on ground-based GNSS slant total electron content (hereafter referred to as STEC). The reconstructed results of E_s structures are validated and analyzed at a high resolution in both space and time. The CIT methods and data used in this analysis are presented in Sections 2 and 3, respectively. Validation of this CIT algorithm is presented in Section 4. Results from three daytime E_s event days are presented and discussed in Section 5. Section 6 gives the conclusion.

2. Computerized Ionospheric Tomography (CIT)

Austen et al. (1988) first proposed the utilization of CIT to reconstruct terrestrial plasma variations from a multitude of irregularly sampled integrated electron density measurements. TEC, an integrated value of ionospheric electron density along the raypath from a satellite to a receiver, can be obtained through the GNSS method with flexibility and efficiency. Since GNSS signal intersects many altitudes of the ionosphere, a 3-D representation of its structure is enabled with CIT, the maturation of which helps develop and improve different CIT methods (Raymund et al., 1990; S. Saito et al., 2017; Ssessanga et al., 2021; Sutton & Na, 1995; Yao et al., 2013). However, the fidelity of most CIT techniques is biased toward reconstructions of the F region, dominant in electron density concentration in the ionosphere, and with the utmost hindrance to transionospheric radio waves. Moreover, because the density contribution of E region to STEC is much smaller when compared to F region, a 3-D reconstruction of minute densities and small perturbation at E region is generally challenging considering the errors in measurements and CIT representation. Additionally, since the thickness of E_s is estimated as ∼2 km, and the TEC enhancement is approximately 1 TECU (1.0×10^{16} el/m^2), lasting for a few tens of minutes (Maeda & Heki, 2014), the success of 3-D E_s reconstruction requires a high spatial and temporal resolution which is computationally cumbersome.

There have been previous efforts to reconstruct the E_s structure using GNSS. For example, Muafiry et al. (2018) used the detrended STEC and a CIT technique with continuity constraints to regularize the least squares inverse problem and separately generated different block solutions of the 3-D structure of daytime E_s over the Kanto and Kyushu Districts in Japan. In each block, the resolutions were 0.16° in the north-south direction, 0.20° in the east-west direction, and 30 km in the up-down direction. From the results, Muafiry et al. (2018) were able to deduce that E_s patches lie at an altitude of ∼100 km, and the horizontal drifts corroborated earlier existing literature. Here, instead of applying ad-hoc constraints to local regional blocks, we use a two-step method that adapts ionosonde and ground-based GNSS observations to reconstruct high-resolution 3-D maps of E_s over the whole midlatitude Japan area. First, we reconstruct a more accurate F region structure and then exploit the solution to estimate the 3-D E_s structure.

2.1. Step 1: F Region Reconstruction

The CIT approach in our analysis follows the voxel-based model, the details of which can be found in a review by Lu et al. (2021) and references therein. The 3-D regional volume to be imaged is divided into n voxels and each voxel (j) is assumed to have an unknown uniform distribution of electron densities x_j. Then, STEC (y_i) corresponding to the satellite-receiver ray signal path is represented as a finite sum over the voxels

$$y_i = \sum_{j=1}^{n} a_{ij} x_j + e_i, \tag{1}$$

where a_{ij} is the length of the ray in intersected voxel (j), otherwise zero; e_i represents both instrumental and representative errors. For many STEC ($\vec{Y}$), Equation 1 is expressible in a compact matrix form as

$$\vec{Y} = \mathbf{A}\vec{X} + \vec{E}. \tag{2}$$

Of course, the fact that $\vec{E}$ exists in Equation 2 and in practice due to satellite-ground receiver geometric constraints and restrictions on exposure time to avoid averaging dynamics, the number of measurements (m) is generally much less than the required number of unknowns (n). Therefore, solving Equation 2 necessitates a different approach than a direct matrix inversion. A rich literature exists on different methods that could be employed to obtain $\vec{X}$ that minimizes the error ($\vec{E}$). Here, a multiplicative algebraic reconstruction technique (MART) from the row-action iterative scheme family is selected (Raymund et al., 1990). This is because MART is memory efficient and ensures positivity, which is mandatory for ionosphere electron densities ($\vec{X}$). The high fidelity, particularly in reconstructing F region densities with MART, has already been demonstrated in Raymund et al. (1990) and Ssessanga et al. (2017). MART is implemented as

$$x_j^{k+1} = x_j^k \left(\frac{y_i}{\langle \vec{a}_i, \vec{X}^k \rangle} \right)^{\lambda_k a_{ij}/\|a_{ij}\|}, j = 1, 2, 3 \cdots, N, \tag{3}$$

where $\vec{a}_i$ represents the ith row vector in matrix $\mathbf{A}$; x_j^k is the jth unknown at the kth iteration; $\langle \vec{a}_i, \vec{X}^k \rangle$ is the simulated TEC, an inner product of the ith row of $\mathbf{A}$ and a column of $\vec{X}$ values at the kth iteration; and λ_k is the relaxation factor selected in range $0 < \lambda_k < 1$, set to 0.2 in this work based on Raymund et al. (1990) and Ssessanga et al. (2017).

The computational procedure in Equation 3 requires an initial guess ($\vec{X}_0$), which highly influences the fidelity and the rate of convergence (Das & Shukla, 2011). This is one of the weak points that MART suffers as a reconstruction algorithm. To improve fidelity, we estimate a smooth $\vec{X}_0$ from the observations (STEC), following the works of Raymund et al. (1990) and Ssessanga et al. (2017): the 3-D regional ionosphere is assumed to be spanned by a set of empirical orthogonal functions (EOFs) $\boldsymbol{\Phi}$. These are derived from an ensemble composed of the ionosphere at different epochs that are representative of the regional ionosphere under different conditions. The ensemble can be generated from an empirical model, here we used the International Reference Ionosphere (IRI)-2016 model, the details of which can be found at Bilitza et al. (2016). To accurately represent F region peak densities, the International Union of Radio Science (URSI) foF2 model recommended for ocean areas, and the newly included improved hmF2 model (Satellite and Digisonde Model of the F2-Layer Height (SDMF2)) (Bilitza et al., 2017; Shubin, 2015; Shubin et al., 2013) were triggered in the IRI settings. For each epoch in one day that was analyzed, $\boldsymbol{\Phi}$ was generated from an ensemble of dimension $n \times 49$, covering daytime (06:00–18:00 LT), sampled at a 2-hr interval, and spanning 7 days centered on a required day. At most, $\boldsymbol{\Phi}$ constituted three orthogonal functions that represented 98% of the ensemble power. From the above setting, the initial guess is represented as $\vec{X}_0 = \mathbf{\Phi}\vec{b}$, where $\vec{b}$ is a set of coefficients to be determined. According to Equation 2, we can obtain

$$\vec{Y} = \mathbf{A\Phi}\vec{b}, \tag{4}$$

and the solution to the initial guess obtained as $\vec{X}_0 = \mathbf{\Phi}(\mathbf{A\Phi})^{\dagger}\vec{Y}$, where $(\mathbf{A\Phi})^{\dagger}$ denotes the pseudo inverse of $\mathbf{A}\boldsymbol{\Phi}$.

2.2. Step 2: E Region Reconstruction

Signal rays from GNSS satellites to ground-based receivers pass through the ionospheric D, E, F regions, and plasmasphere with significantly different contributions to daytime STEC. We assumed the electrons in the signal ray paths concentrate in altitude ranging from 80 to 1,000 km, since the D region is generally populated with relatively weakly ionized plasma (Kelley, 2009), and the plasmasphere, particularly during the summer daytime in the northern hemisphere, varies mildly and contributes up to 10% to the ground GNSS vertical TEC in the mid-latitude area (Belehaki et al., 2004; Yizengaw et al., 2008). Therefore, we can deduce the E region contribution as $STEC_E \approx STEC - STEC_F$. For each ray, at a specific epoch, $STEC_F$ was estimated as an integral of densities along the line of sight through step-1 3-D reconstructed ionosphere covering altitudes 180–1,000 km. The $STEC_E$ residues are then utilized in the reconstruction of the E region structure covering 80–180 km in altitude.

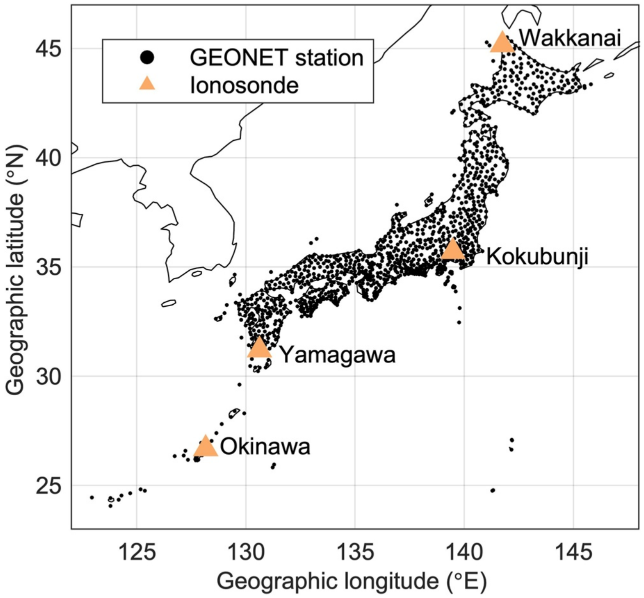

Figure 1. Distributions of GEONET stations (black dots) and ionosondes (yellow triangles).

Due to the relatively small thickness of the E_s structure, a high vertical resolution is needed to resolve the density distribution. However, in ground-GNSS data CIT analysis, the accuracy in the vertical domain is low due to the lack of horizontal ray paths (Razin & Voosoghi, 2016). To vertically constrain the solution, we again employ EOFs, but following a different procedure from that discussed in step-1: different electron density ensembles ($Ens(t_{hr})$) were used to generate a family of subsets of EOFs(t_{hr}) assumed to span the E region 3-D space at intervals/windows (t_{hr}) of 1 hr, covering the period 06:00–18:00 LT. The $Ens(t_{hr})$ members were based on a Chapman model function

$$N_e = N_m * \exp\left(0.5 * \left(1 - \frac{h-h_m}{H} - \exp\left(-\frac{h-h_m}{H}\right)\right)\right), \tag{5}$$

which we could adjust so that the E_s layer mimics a thickness of ~2 km as depicted in rocket (Whitehead, 1989) or GNSS radio occultation observations (Zeng & Sokolovskiy, 2010). h, H, N_m and h_m represent the height of any desired point along the profile, the scale height, E_s intensity, and its height location (*hmEs*), respectively. To compose each $Ens(t_{hr})$, N_m , and h_m were assumed from Gaussian distributions with moments (mean and standard deviation) derived from manually scaled ionosonde E_s observations (*foEs* and *hmEs*) covering 30 days. The threshold for E_s occurrence was 5 MHz (Aarons & Whitney, 1968). Yellow triangles in Figure 1 show a network of four ionosondes considered in the analysis. Based on the work of Ssessanga et al. (2017), who utilized the same network of ionosondes and GNSS receivers, Kokubunji ionosonde was found to be located in the region of most data points and best CIT reconstructions. Thus, because the aim is to additionally reconstruct a clear E_s height variation, Kokubunji ionosonde data were used in determining the standard deviation (σ) of the h_m distributions as follows: The E_s height within the interval, t_{hr}, was assumed to nearly remain stable from one day to the next (Šauli & Bourdillon, 2008). Then, for each t_{hr} and ionosonde in the network, we computed a mean (μ_h) and standard deviation (σ_h), from which we derive the standard deviation of h_m Gaussian distribution for each ionosonde based on Kokubunji *hmEs* (h_m^{ko}) as

$$\sigma = \begin{cases} 0.5\sigma_h, & |h_m^{ko} - \mu_h| \leq 0.5\sigma_h \\ 2\sigma_h, & |h_m^{ko} - \mu_h| \geq 2\sigma_h \\ \sigma_h, & otherwise. \end{cases} \tag{6}$$

To further emphasize the dominance of data from a region of most data points, in an $Ens(t_{hr})$ of 1,000 members, the contribution from different ionosonde distributions was reduced with increasing distance away from the region of most data points: Kokubunji (40%), Yamagawa (30%), Okinawa (20%), and Wakkanai (10%).

The challenge in using the Chapman function was an appropriate selection of the scale height(s) H that would reproduce the E region structure and the exact altitude of electron density peak. Heuristically, better results were obtained when some vectors in a selected EOFs(t_{hr}) set were either emphasized or damped by a factor

$$P_i = e^{-EOF(t_{hr})_i/SF}, \tag{7}$$

where P_i is the scale size of ith radial orthogonal basis vector in EOFs(t_{hr}) and SF is a learned scale factor. Note that we are not changing the direction of the basis vectors but rather the amplitude; this analysis is further discussed in Section 4.2.

To reconstruct the 3-D E region structure ($\vec{X}_E^{t_e}$) at a particular epoch (t_e), we solved a system

$$\vec{Y}_E^{t_e} = \mathbf{A}_E^{t_e}\vec{X}_E^{t_e} + \vec{E}_E^{t_e} \tag{8a}$$

$$\vec{Y}_E^{t_e} = \mathbf{A}_E^{t_e}\mathbf{M}(t_{hr})\vec{b}_E^{t_e} + \vec{E}_E^{t_e},\ \vec{X}_E^{t_e} = \mathbf{M}(t_{hr})\vec{b}_E^{t_e} \tag{8b}$$

$$\vec{Y}_E^{t_e} = \mathbf{C}_E^{t_e}\vec{b}_E^{t_e} + \vec{E}_E^{t_e},\ \mathbf{C}_E^{t_e} = \mathbf{A}_E^{t_e}\mathbf{M}(t_{hr}) \tag{8c}$$

where all symbols mean the same as in step-1, with subscript E implying E region. $\mathbf{M}(t_{hr})$ is an orthogonal matrix formulated using a subset of EOFs(t_{hr}) representing 98% of the variation in $Ens(t_{hr})$, and t_{hr} is the time interval that includes t_e. $\vec{b}_E^{t_e}$ are coefficients to be determined that define different optimal combinations of radial EOFs at each horizontal grid point.

To adequately solve Equation 8, the singular value decomposition (SVD) method was selected because of its numerically stable properties (Fan & Ma, 2014). The major disadvantage of SVD is the high computation cost; however, because the problem is transformed into EOF space, and the reconstructions are limited to the E region, the dimensionality of the problem is significantly reduced to a desktop CPU manageable setting. If matrix $\mathbf{C}_E^{t_e}$ is of dimension p by q, then through SVD decomposition

$$\mathbf{C}_E^{t_e} = \mathbf{U}\mathbf{D}\mathbf{V}^T, \tag{9}$$

where $\mathbf{U} \in \mathbb{R}^{p\times p}(\mathbf{V} \in \mathbb{R}^{q\times q})$ is an orthonormal normal matrix composed of left (right) singular vectors of $\mathbf{C}_E^{t_e}$, associated with singular values or weights contained in a rectangular diagonal matrix $\mathbf{D} \in \mathbb{R}^{p\times q}$; T represents matrix transpose. Once the decomposition is attained, the problem is simplified to an exercise of selecting an r-dimensional sub-space of singular vectors and weights, that best represent $\mathbf{C}_E^{t_e} \approx \mathbf{U}_r\mathbf{D}_r\mathbf{V}_r^T$, such that

$$\vec{b}^{t_e} \approx \mathbf{V}_r\mathbf{D}_r^{-1}\mathbf{U}_r^T\vec{Y}_E^{t_e}, \tag{10}$$

having used the identity $\mathbf{U}\mathbf{U}^T = \mathbf{I}$ and $\mathbf{V}\mathbf{V}^T = \mathbf{I}$. Based on $\vec{X}_E^{t_e} = \mathbf{M}(t_{hr})\vec{b}_E^{t_e}$ in Equation 8b, the final solution is

$$\vec{X}_E^{t_e} \approx \mathbf{M}(t_{hr})\mathbf{V}_r\mathbf{D}_r^{-1}\mathbf{U}_r^T\vec{Y}_E^{t_e}. \tag{11}$$

A more detailed description of SVD and its application to inverse problems can be found in Gołub and Van Loan (1989).

3. Data

Based on a method discussed in Ma et al. (2014), the STEC data used in this study were derived, with a time resolution of 30 s, from dual-frequency GNSS observations recorded by the GEONET (GNSS Earth Observation Network): a nationwide dense GNSS array in Japan consisting of more than 1,200 receivers. Nearly 5,000 satellite-receiver paths are recorded every 30 s (A. Saito et al., 1998). Black dots in Figure 1 denote the distribution of GEONET stations. The network is ideal for imaging structures such as E_s irregularities since the spacing between stations is less than 25 km (Maeda & Heki, 2014). Receiver and transmitter instrumental biases were estimated following Ma and Maruyama (2003). Errors due to multipath effects were mitigated by limiting the analysis to STEC values with elevation angles greater than 30°.

Ionosondes are among the most accurate tools for probing the Earths' plasma density, thus typically used for calibrating other more complicated observation methods (Ssessanga et al., 2017). Yellow triangles in Figure 1 show a network of four ionosondes used in our study, located at Kokubunji (35.71°N, 139.49°E), Yamagawa (31.20°N, 130.62°E), Wakkanai (45.16°N, 141.75°E), and Okinawa (26.68°N, 128.15°E). From the NICT (National Institute of Information and Communications, in Japan) ionosonde database, both automatic and manually scaled ionosphere parameters are accessible, but the latter with a lower time resolution (1 hr) and better accuracy. Because our study is on small-scale structures that demand a certain degree of preciseness, we selected manually scaled observations for analysis.

Spaceborne GNSS radio occultation (RO) provides well-distributed ionospheric soundings that complement ground-based observations. An example of RO missions includes COSMIC (Constellation Observing System for Meteorology, Ionosphere and Climate) 1/2 launched in 2006 and 2019, respectively, with good coverage of low- and midlatitude regions (Hsu et al., 2018). The mission produces between ∼2,000 and ∼4,000 good soundings of the ionosphere per day. The data are archived in order of accuracy: reprocessed, post-processed, and real-time. For accuracy purposes, the reprocessed ionosphere density profiles (“ionPrf”) provided by the CDAAC

(COSMIC Data Analysis and Archive Center) are used in our validation. More details about COSMIC and data processing are available at https://www.cosmic.ucar.edu/.

4. Algorithm Validation

The 3-D region to be analyzed covered 24°N–46°N in latitude, 122°E–146°E in longitude, 80–1,000 km in altitude. In step-1 (step-2), the total number of voxels were 24,288 (330,000), with the resolution set to 1° (0.4°) in horizontal and 20 km (1 km) in altitude. To avoid reconstructions of highly irregular plasma fluctuations due to geomagnetic storms, particularly in the F region, analysis data were filtered to only include days when the absolute values of the Dst index were less than 30 nT (Mao et al., 2010). Under such smooth conditions, during daytime at midlatitudes, a well-developed and highly conducting E region limits polarization electric fields that could facilitate the E-F coupling (Kelley, 2009). Therefore, to avoid sharp transitions, from a high-resolution (1 km) E region to a coarse (20 km) F region, we assumed that E and F regions are separable under different implicit periods of stationarity; 15 and 1.5 min in step-1 and step-2, respectively. This setup reduced the size of the inverse problems to a Desktop manageable setting with 8 gigabytes of memory. Indeed, the reducing size of systems improved the condition number/stability and the convergence of the iterative procedure to within 7 min.

4.1. Validation in Step 1

Before reconstructions with observational data, we performed a simulation to analyze challenges in reproducing a consistent picture of the F region if enhanced prolate density-like structures existed in the E region. Similar to the results obtained in Ssessanga (2018), the reconstructions were modest, but when a large percentage of the utilized rays traversed the prolate structures, the MART algorithm subtly reconstructed the E-region features in the F-region. Kunitsyn and Tereshchenko (2003) also detected this underperformance by MART. The authors found that if features are in a region of low density (E-region), MART tended to reconstruct them toward areas of high concentration, around $hmF2$ point. Therefore, to mitigate the F-region contamination, data ($\vec{Y}$) in Equations 3 and 4 were filtered to remove rays that traversed sizable E_s structures: the rate of TEC index (ROTI < 0.1) (Mungufeni et al., 2021), defined as the standard deviation of the change rate of TEC, was used in filtering process (Pi et al., 1997). Figure 2a illustrates an example of synchronous changes in GNSS STEC and ROTI on DOY 141, 2010. Fortunately, during this event, the satellite (Sat) in view, GPS PRN 29, crossed the Kokubunji ionosonde station location, a yellow triangle in Figure 2b. The solid black line is Sat 29 ground trace and the black dot represents the ionospheric pierce point (IPP) at 17:15 LT (LT = UT + 9). The synchronous pulse-like changes in STEC and ROTI in Figure 2a, are observed to occur at the same epoch, 17:15 UT, when a clear E_s layer at altitude ∼106 km is recorded in ionosonde observations in Figure 2c. Therefore, changes in ROTI can be a filter or detection for plasma inhomogeneities. Finally, to reduce computational cost and avoid redundancy as in S. Saito et al. (2017), only data from 280 stations were selected for calculation in step-1.

In Figure 3, a control data set from more than 100 GEONET receivers is used to assess the accuracy of the reconstructed results. The subplots represent IRI model (a), initial guess using EOFs (b), and MART solution (c), respectively. The three sets of results show improvement in each step (a–c), hence satisfying the requirement for MART quick convergence and good fidelity as discussed in Section 2.1. To evaluate the effectiveness and reliability, metrics of mean absolute error (MAE) and root mean square error (RMSE) are introduced to specify the degree of dispersion of the sampling error (Xiong et al., 2021), which are computed as follows:

$$MAE = \frac{1}{N}\sum_{i=1}^{N}|y_r - y_o| \tag{12}$$

$$RMSE = \sqrt{\frac{1}{N}\sum_{i=1}^{N}(y_r - y_o)^2} \tag{13}$$

where N is the amount of the reconstructed values, y_r and y_o are the reconstructed and observation values, respectively. The unit of MAE and RMSE is TECU.

Discrepancies between estimations and observations are eminent when the ionosphere is generated from the IRI model; MAE and RMSE are 2.65 and 2.89 TECU, respectively. After introducing EOFs, the MAE and RMSE

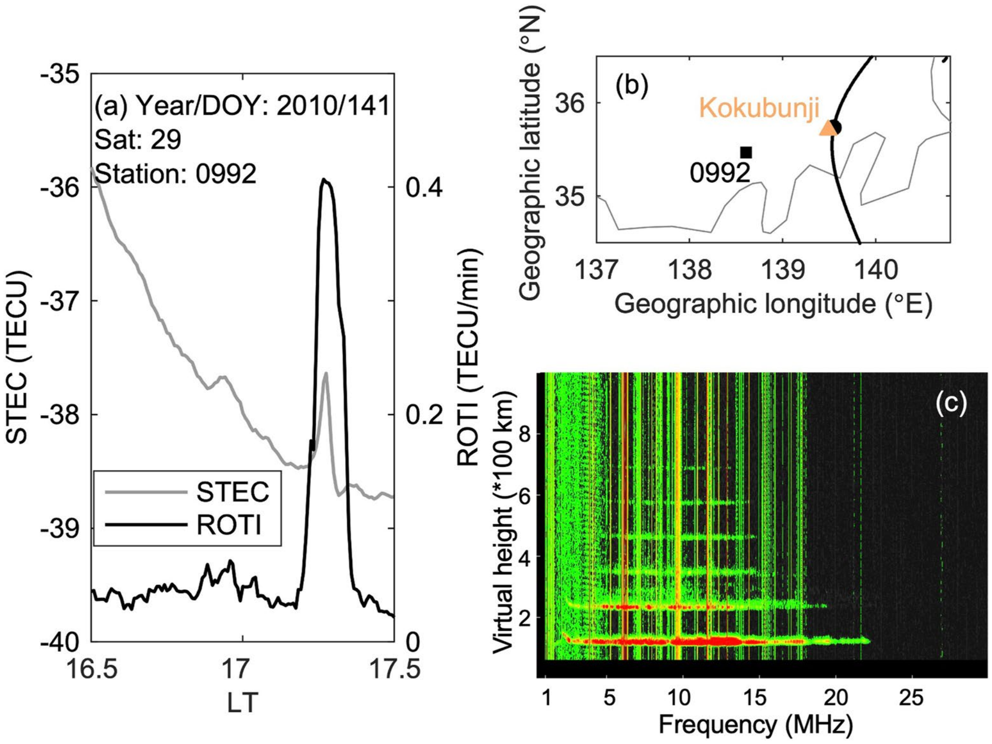

Figure 2. Observations from GNSS and ionosonde near Kokubunji area, where the E_s signature happens around 17:15 LT, DOY 141, 2010. (a) Timeseries of STEC anomalies (gray) and ROTI (black). (b) Trajectories of IPPs at 106 km from station 0992 to Satellite (Sat) 29 passing through the Kokubunji ionosonde (yellow triangle), where the black square and dot represent the location of 0992 receiver and IPP at 17:15 LT, respectively. (c) The 17:15 LT ionogram at Kokubunji, where the highest foEs observed is ∼20 MHz.

decrease to 1.88 and 2.20 TECU. The fitted line gradient improves from 0.49 to 0.78; the higher correlation between reconstruction and observation suggests a confident initial guess was estimated from GNSS observations with EOFs. By applying MART, results converged to minimize the errors, where the MAE and RMSE are 0.93

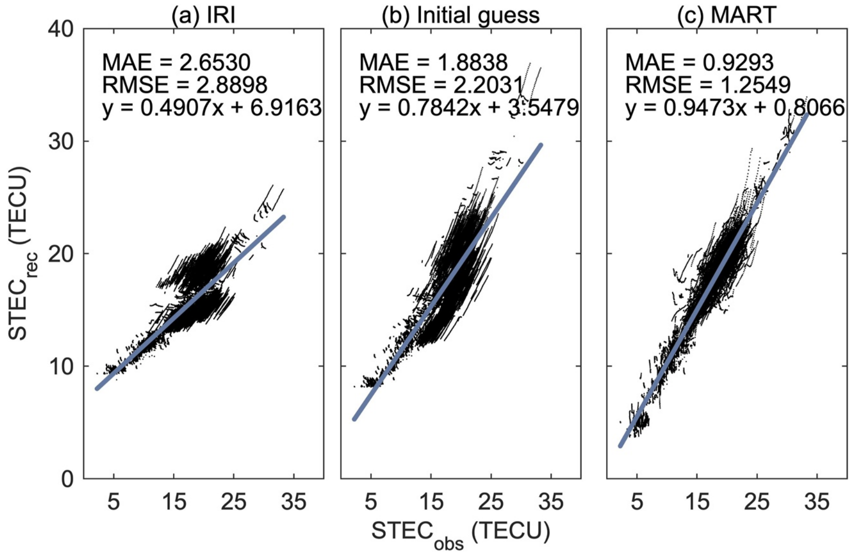

Figure 3. A Scatter of observation and estimates of STEC values during 17:22–17:37 LT, on DOY 141, 2010. Subplots (a–c) represent IRI-2016, initial guess using EOFs and MART, respectively. The least squares regression lines are in blue, with horizontal as x and vertical y. MART results fit the observations best.

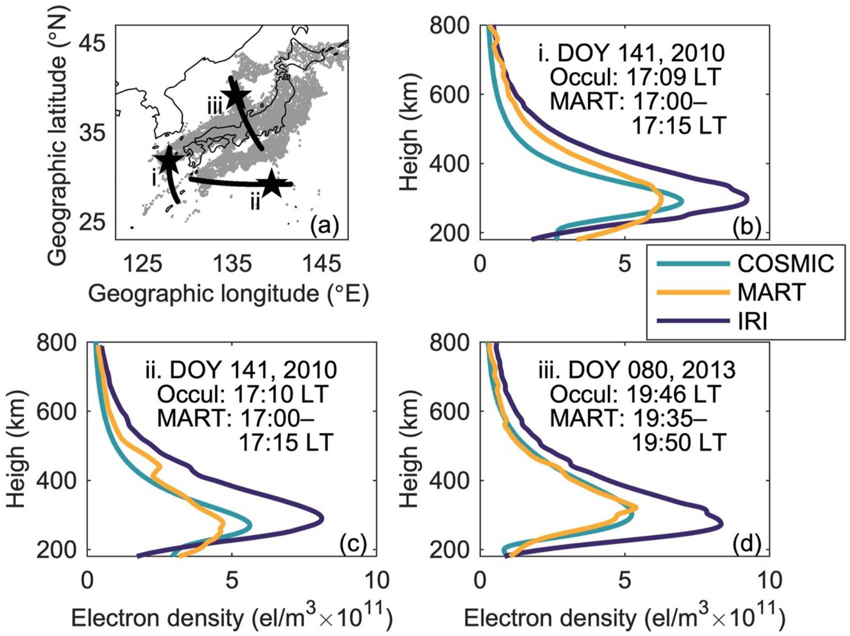

Figure 4. (a) Black solid lines are traces of COSMIC occultation tangent points, black stars are locations of maximum electron density along each trace, and gray dots represent the distribution of ionospheric pierce point (IPP) at 17:10 LT on DOY 141, 2010, at 350 km altitude. (b–d) Comparison of COSMIC constellation vertical electron density profiles (green) with IRI model (purple) and tomography (yellow).

and 1.25 TECU, respectively. The gradient of the fitted line has been improved to 0.95, which suggests the reconstructed STEC are in good agreement with the observed STEC. This good consistency indicates the ionosphere is reconstructed with fidelity.

In Figure 4, COSMIC constellation electron density vertical profiles are compared to the IRI model and reconstructed results (obtained as a solution to Equation 2, while using MART and a calibrated initial guess). Although RO data distribution is globally good, events that locally consistently cover a particular region are difficult to find. Thus, after an exhaustive data search, the presented three RO events fit our analysis best. The comparison is along the geographic locations of the occultation tangent points, shown as solid black lines labeled i, ii, and iii, in Figure 4a. Black stars are geographic locations of the maximum electron density along each profile trace. During analysis, the reconstructed ionosphere was assumed stationary for 15 min, with the center point as the epoch to the maximum electron density points. Gray dots show an example of the distribution of GNSS rays ionospheric pierce points (IPPs) at the 350 km altitude (epoch is 17:10 LT, DOY 141, 2010). Figures 4b–4d are density profiles corresponding to each trace in Figure 4a. The vertical scale is limited to altitudes 180–800 km, where occultation profiles have good accuracy. Compared to the IRI model, the reconstructed profiles (mainly *hmF*2 and *NmF*2) correlate better with the occultation densities, specifically over central Japan with the densest IPP distribution (refer to trace [iii] and Figure 4d). Outside central Japan, see traces (i) and (ii) and the respective corresponding profiles in Figures 4b and 4c, deviations between COSMIC and reconstruction maximum electron density are more pronounced consequent to the sparse IPP distribution. Nonetheless, the reconstructions were on average ∼30% more accurate than IRI electron density estimation.

4.2. Validation in Step 2

Analogous to step-1, we carried out a simulation analysis to assess the validity of our reconstructions in the E region. Kokubunji ionosonde observation at 17:30 LT on DOY 141, 2010 were used as a reference in the E_s simulation, with Equation 5 as the model function. Outside the E_s domain, electron densities were computed from the IRI-2016 model. The intensity of E_s patchy layers was set to 5×10^{12} el/m^3 (*foEs* ≈ 20 MHz), at altitude 106 km, with the longest strip stretching ∼8° in East-West (E-W) and 0.4° in North-South (N-S). Figure 6a shows the simulated E_s strips. Note that the strips are intentionally put at different latitudes to assess the fidelity across

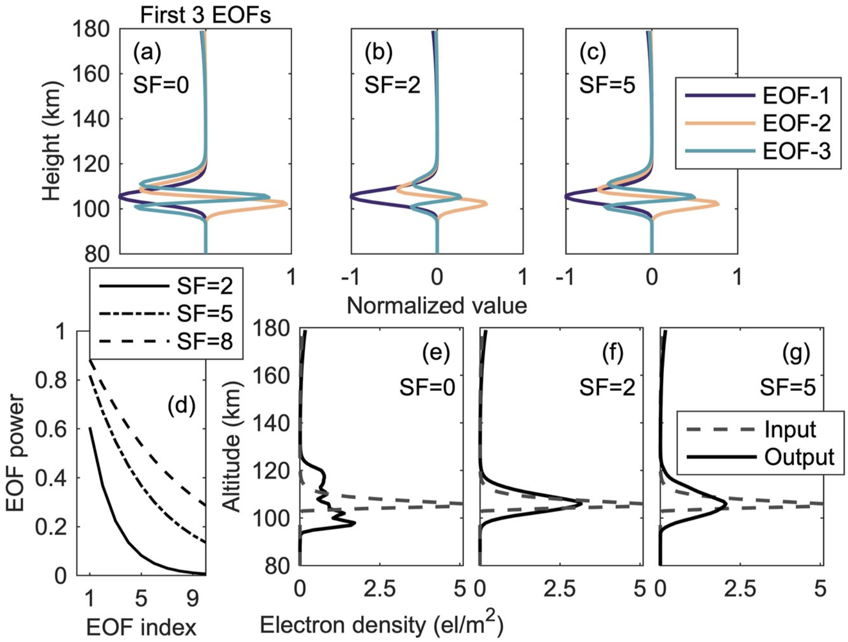

Figure 5. (a–c) The largest three EOFs modified using different scale factors (SFs) at 17:30 LT on DOY 141, 2010. (d) The decay rate of EOF scale size as function EOF position in the EOF subset. (e–g) Reconstructions of the simulated E_s structures with largest amplitude, while considering different SFs.

the map. The synthetic STEC for analysis were then generated as an integral of electron densities along the ray paths determined from the observation geometry of GNSS satellites and more than 1,200 receiver stations from the GEONET. Black dots in Figure 6b show the distribution of the GNSS rays IPPs at the E_s height of 106 km, corresponding to the synthetic STEC data points.

Before discussing the 3-D simulation results, we use this simulation and revisit the discussion in Section 2.2 to elaborate on the significance of scaling EOFs, as illustrated in Figure 5. Although the 98% representation of the original ensemble was constituted by 10 EOFs, for clarity, we have presented only the first three EOFs representing 43.42%, 21.72%, and 12.21% of the ensemble variations. Subplots (a–c) show the modification in the amplitude of EOFs as SF is varied. In the lower plate: the far left subplot (d) illustrates different scale size decay rates (using different SFs) as a function of position (“importance”) of an EOF vector in the selected EOF subset. Still, in the lower plate, the three subplots (e–g) showcase an example of the input (dashed gray line) and reconstructed (solid black line) E_s-layer with largest amplitude using different SFs. Before any scaling (SF = 0), the reconstructed profile has multiple peaks artifact. As the SF increasingly varied, the artifact disappears and then slowly reappears when the SF > 5; most probably due to the combined EOFs vectors nearly representing the same space as EOFs at SF = 0. For this analysis, SF = 2 was considered the best option: the artifacts are no more, and the profile thickness and height are in good agreement with the input, although we had to trade off some accuracy of the underperformance in amplitude estimation. Subsequent to this analysis, all E_s reconstructions henceforth are obtained with a scaling of SF = 2.

Back to the 3-D simulation reconstructions in Figure 6, the minimum boundary conditions and GNSS-receiver geometry constraints limit observations at areas such as Hokkaido (> 40°N) and Kyushu (< 32°N). Indeed, the strip structures at ∼32°N and ∼40°N are reconstructed with shorter lengths. As expected, the area bound 33°N–40°N and 131°E–141°E with dense IPPs distribution exhibits the best fidelity. The structures with a separation of ∼1° in N-S are distinctively reconstructed. In the radial dimension, the reconstructed electron densities, shown in subplot (d), are well distributed between 100 and 110 km, and the peak is consistent with the input *hmEs* of ∼106 km.

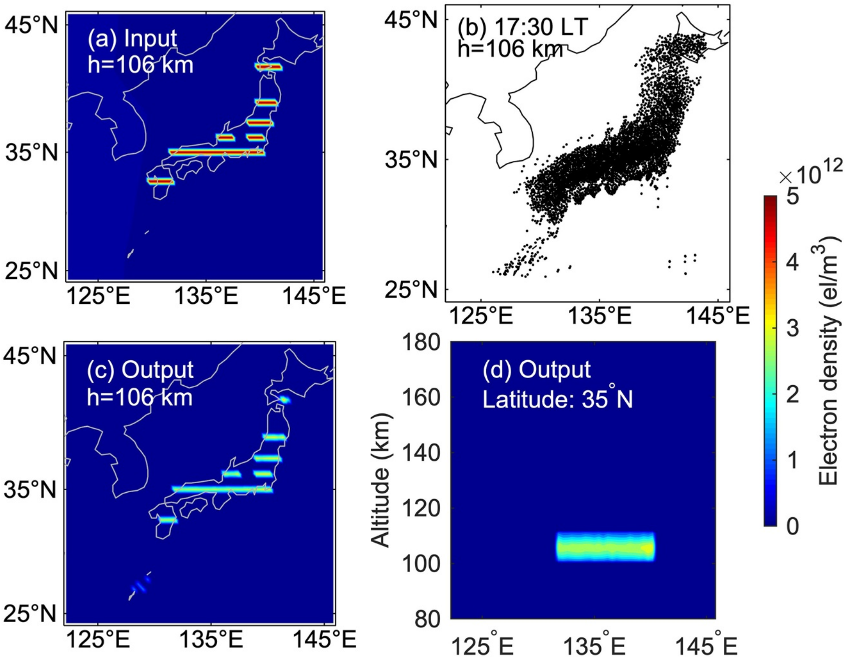

Figure 6. (a) 2-D map of input irregularities at 106 km. (b) Distribution of IPPs at 17:30 LT, DOY 141, 2010, at 106 km. (c) 2-D map of the reconstruction at 106 km. (d) Vertical structure of reconstructed electron densities at ~35°N. The best reconstruction is around central Japan.

5. Results and Discussion

In what follows, we shall now use the developed technique to analyze the morphology of E_s during different events in 2007, 2010, and 2020. The 2-D ROTI maps for these three events are shown in Figures S1–S3 of Supporting Information S1. The event on DOY 141, 2010 was previously analysed in 2-D by Maeda and Heki (2014), and thus we can further validate our reconstructions by comparing the two results. The focus is on the region of high fidelity as elaborated in the simulation analysis. To ensure that our reconstructions were mainly due to E_s variations and reduce the computation cost, the data utilized hereafter were filtered to only include STECs with ROTI ≥ 0.1; refer to Figure 2.

5.1. Event of DOY 141, 2010

As a measure of accuracy, in Figure 7, we have reconstructed the E_s structures detected by the Kokubunji ionosonde on DOY 141, 2010. The upper left subplot (a) shows a horizontal 2-D slice at altitude 106 km, epoch 17:30 LT when E_s was intense in horizontal scale. The yellow triangle represents the location of Kokubunji ionosonde. The horizontal frontal structure is elongated in E-W, expanding over several hundred kilometers, which agrees with the results in Maeda and Heki (2014). The right upper plot (b) is a vertical slice through the E_s structure at 36°N, which indicates the electron density anomalies are concentrated at around 106 km altitude and do not appear in other layers that are outside the E_s height range. In the lower subplot (c), reconstructed E region vertical electron density profiles with maximum E_s intensity at the Kokubunji area (35.2°–36.4°N, 138.8°–140.0°E) are combined at a resolution of 3 min to form a timeseries image covering 16:30 to 18:00 LT. Yellow triangles indicate the Kokubunji ionosonde $hmEs$, ought to have remained constant for the entire duration, at ~106 km, as reflected by the white dashed line from reconstruction results. An intensified E_s is eminent through this period. Based on the equation $foEs = \sqrt{80.6 * NmEs}$ (Haldoupis, 2019), at around 17:15 LT, the reconstructed $foEs$ (14.29 MHz) is about 6 MHz smaller than ionosonde observations (~20 MHz) as shown in Figure 2c. This was expected given the results in the simulation analysis (see $SF = 2$ lower-middle subplot in Figure 5). Nonetheless, the reconstructions are still sufficient to draw significant physical underpinnings about E_s.

Figure 8 shows 2-D horizontal electron density distribution maps during 16:30–18:00 LT, on DOY 141, 2010. The slices are at altitudes of maximum E_s within the grid. The time resolution for the two middle rows is higher

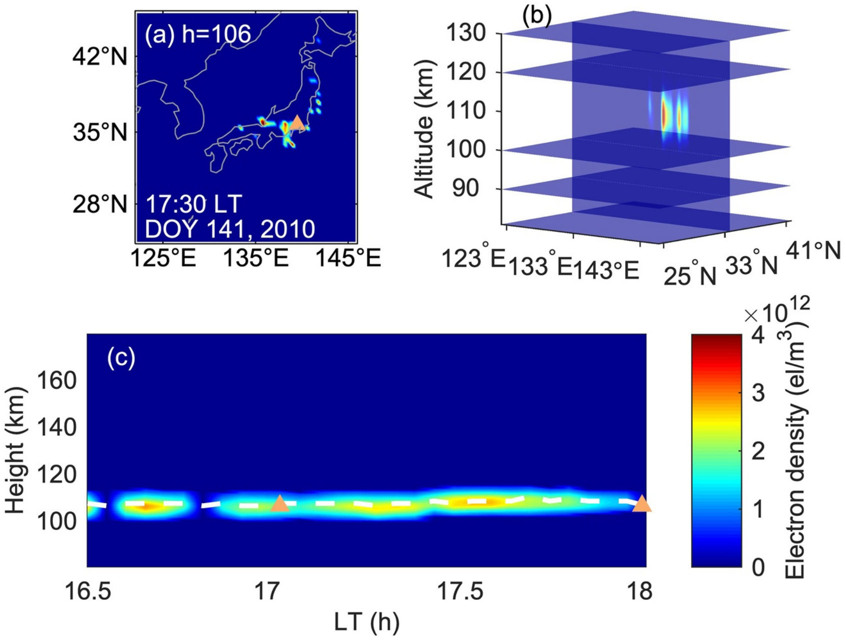

Figure 7. (a) 2-D tomography results at 106 km at 17:30 LT on DOY 141, 2010, yellow triangle represents the location of Kokubunji ionosonde. (b) The vertical slice through the reconstructed structure of reconstruction, at 36°N. (c) Time variation of the vertical structure at Kokubunji area. Yellow triangles and the white dashed line represent the *hmEs* from Kokubunji ionosonde and reconstructions, respectively.

to showcase the E_s horizontal evolution. White and gray arrows show the drift and expansion directions of the E_s structure, respectively. E_s patches start appearing at ∼17:00 LT, and the frontal structure becomes obvious at ∼17:20 LT in central Japan (∼ 35°N), with a distinct alignment in E-W. At around 17:24 LT, on the south side of the main structure, a northwest-southeast (NW-SE) aligned substructure starts to accumulate. The different

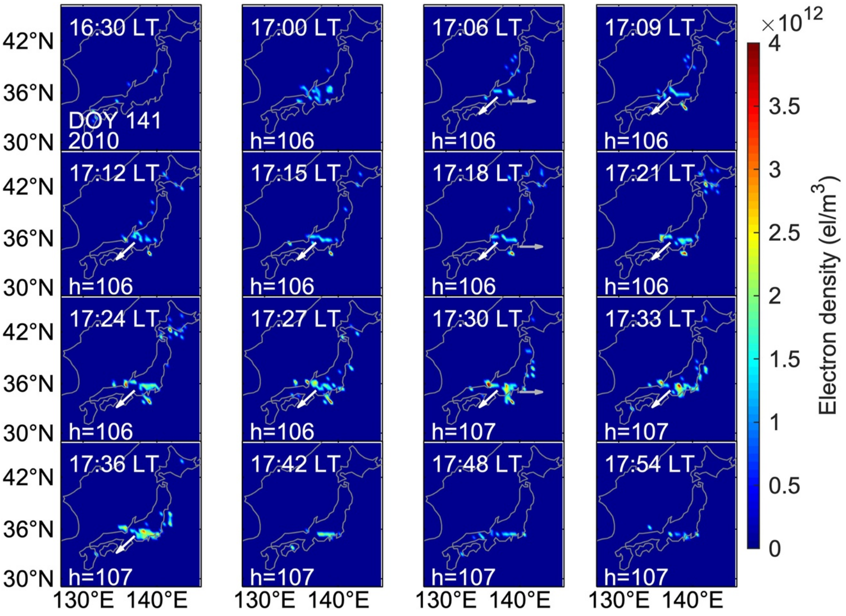

Figure 8. Snapshots of electron density anomaly maps at the height of maximum E_s, at various time epochs from 16:30 to 18:00 LT on DOY 141, 2010. White and gray arrows indicate the E_s drift and expansion direction, respectively. In the two middle rows, when E_s was profound, the time resolution is increased to 3 min to adequately capture the time evolution of plasma.

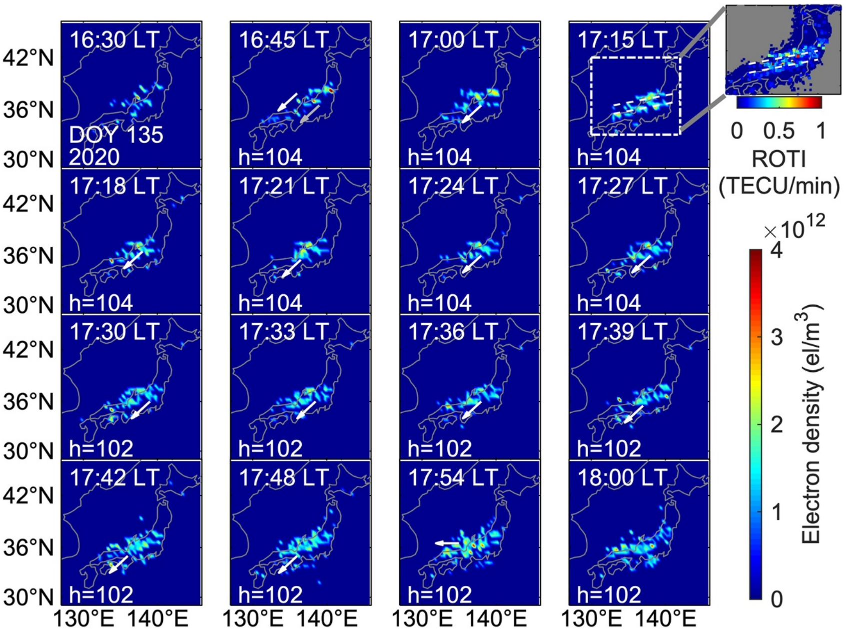

Figure 9. Same as Figure 8 but for DOY 135, 2020. The subplot in the upper right corner shows the ROTI distribution in the selected area (within the white dot-dashed lines) at 17:15 LT, where the white dashed lines indicate the azimuth of the E_s frontal structure alignment.

alignment direction and morphology may be related to the internal perturbations, where the velocity and density of each patch are not homogeneous. Of course, the accuracy of STEC and spatial resolution in this analysis is not sufficient to resolve such density inhomogeneity. However, Sun et al. (2020) have analyzed the high Doppler spectral width of the radar echoes in E_s, which indicated severe perturbation inside the layer. The band-like main structure reach maximum in scale at ∼17:30 LT, which can be extended to ∼400 km in E-W. E_s structures start to dissipate after around 17:42 LT, the lifetime of this strong E_s with *foEs* exceeding 20 MHz can reach approximately 30 min. We calculated the approximate speed of the E_s peak every 20 min and found the E_s patches on the east side to have an eastward velocity of ∼60 m/s, which corroborates the 2-D TEC map analyses of the same event by Maeda and Heki (2014). During this period, the frontal E_s structure has an obvious southwestward migration, with a mean speed of ∼75 m/s.

5.2. Event of DOY 135, 2020

Figure 9 shows the horizontal electron density distribution maps to this E_s event (16:30–18:00 LT). Different from the event in Figure 8, E_s patches appear enhanced near 39°N just after 16:30 LT, elongated in weak northeast-southwest (NE-SW), and more intense. At 16:45 LT, a frontal structure aligned in E-W and stretching ∼150 km is eminent. At ∼17:15 LT, two parallel frontal structures aligned in NE-SW with a separation of ∼1° are formed, as confirmed by the ROTI distribution in the upper right subplot. The white dashed lines indicate the azimuth of the E_s frontal structure alignment. Similar cases with two individual E_s bands were also reported in Sun et al. (2020), which could be generated sequentially by the continuously modulated wind shear system (Sun et al., 2021). From 17:00 to 17:30 LT, these two frontal structures have the same southwestward migration, with a mean speed of ∼70 m/s. After 17:30 LT, the E_s speed increased to ∼100 m/s and the motion component in the west direction became increasingly dominant. The E_s peak density is located at an altitude of ∼104 km in the beginning and then decreases to ∼102 km, which agrees with *hmEs* observed from Kokubunji ionosonde (102 km) at 17:00 LT. For this event, the E_s structure can be elongated roughly 600 km in E-W direction.

5.3. Event of DOY 151, 2007

Figure 10 shows slices of 2-D horizontal E_s reconstructions at E_s peak altitudes. The yellow triangles represent the location of Kokubunji ionosonde. In the central Japan, obvious frontal structures of E_s aligned in E-W occur

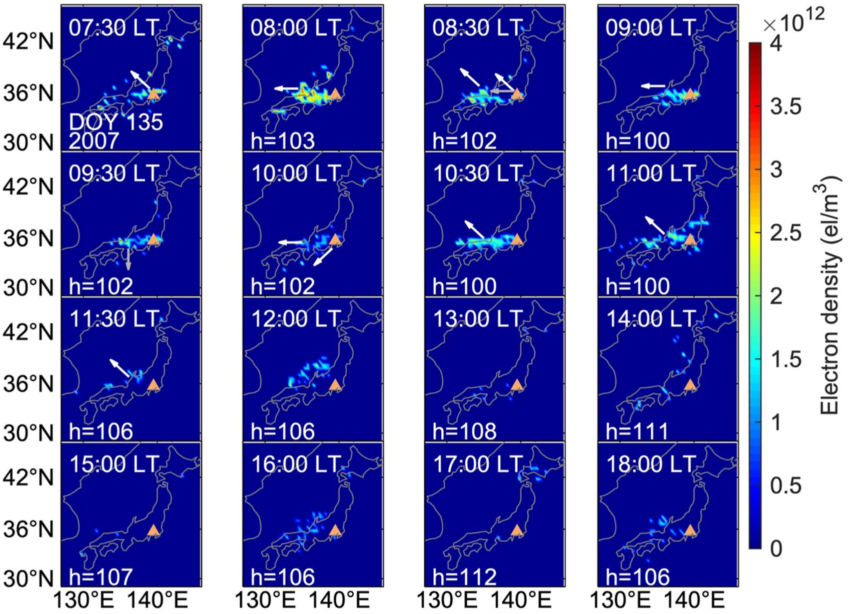

Figure 10. Snapshots of electron density anomaly maps at the height of maximum E_s, at various time epochs from 07:30 to 18:00 LT on DOY 151 2007. White and gray arrows indicate the E_s drift and expansion direction, respectively. Yellow triangle indicates the location of Kokubunji ionosonde.

after sunrise from ~07:30 to 11:00 LT. In this period, the horizontal scale of E_s frontal structure can reach 400 km in E-W. At 08:00 LT, when E_s structure shows high intensity, the main E_s structure is aligned E-W and spanning over hundreds of kilometers, but the fine constituents of this patch seem to have a strong preference of alignment in the NW-SE direction. This is the first result that clearly shows the morphology of structures that form such larger E-W structures, and future investigation of this phenomenon is vital to infer information on the formation and mechanisms of large E_s patches.

Based on Figures 8–10, also observed is the main azimuth drift in the northwest (morning) and southwest (afternoon) directions, which are consistent with the conclusions from observations in Maeda and Heki (2015) and simulations in Tsunoda et al. (2004) and Yokoyama et al. (2009). From the upper-atmospheric wind data recorded by the MU radar (located at 34.9°N, 136.1°E; data accessible at http://www.rish.kyoto-u.ac.jp/mu/meteor/) during this event, the directions of reconstructed E_s and neutral winds at altitudes 100–105 km are consistent. Therefore, we think the background-neutral wind is a dominant factor in the dynamics of observed strong E_s structures.

To manifest the variation of *hmEs* and *foEs* at Kokubunji area, in Figure 11, vertical electron density profiles with maximum E_s intensity from reconstructions in this region were used to generate the timeseries image at a resolution of 6 min. White dashed lines show the reconstructed E_s layer variation with time. The length of the error bars is *hmEs* standard deviation used in generating the ensemble from which EOFs applied to a particular time window are computed. To vividly assess the accuracy of the height undulance reproduced in the reconstructions, *hmEs* (solid yellow triangles) obtained from the Kokubunji ionosonde station are included in the plot. At a height range ~95–110 km, during ~07:15–11:15 LT, a frontal E_s structure develops. The E_s layer of sizable amplitude appears between 08:00 and 09:15 LT, which is consistent with the *foEs* variation observed by Kokubunji ionosonde. From 7 to 11 LT, the reconstructed E_s-layer is observed to descend in altitude, which can be attributed to the semidiurnal and diurnal tides (Haldoupis et al., 2006; Mathews, 1998). Hence, atmospheric tidal winds might be an influential factor in the formation and dynamics of daytime midlatitude sporadic E.

The merits of the newly developed technique are apparent in tracking the radial-time variation of the E_s structure, indicated as a white dashed line in Figure 11. The reconstructed E_s structures with a high temporal resolution during 06:30–12:30 LT are shown in Figure S4 of Supporting Information S1. Comparison of the reconstructed curve and observed *hmEs* indicates that our technique can capture the relative time-vertical motion of the E_s-layer, with a mean error of ~4 km; the ensembles in generating EOF subsets may not fully capture some erratic E_s inhomogeneities, for example, when *hmEs* approaches or exceeds 120 km at 14:00–15:00 LT. There is no literature

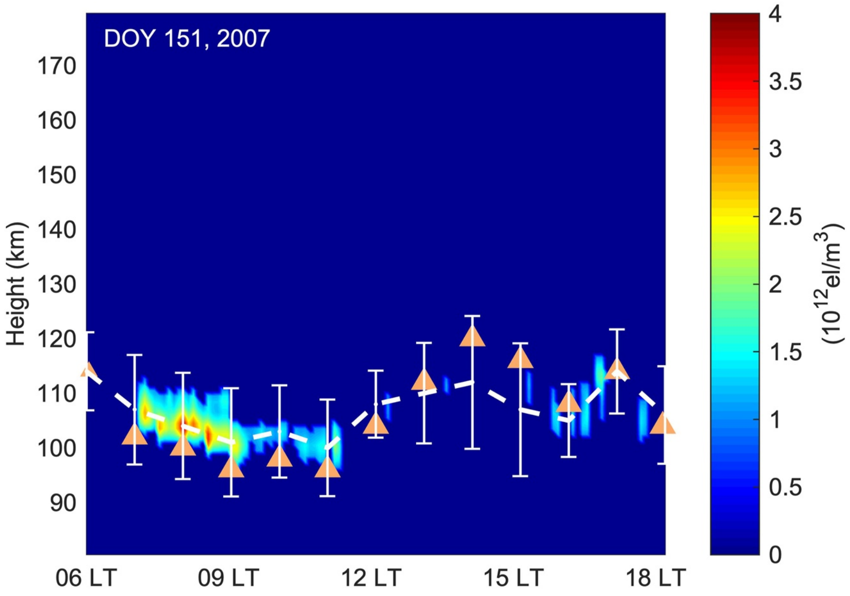

Figure 11. The vertical electron densities at Kokubunji area on DOY 151, 2007. Yellow triangles represent *hmEs* observed by ionosonde at Kokubunji, white dashed lines show the reconstructed E_s layer variation with time, and the length of the error bars indicate standard deviation corresponding to the ensemble used in generating the EOFs applied for a particular epoch.

we can find relating to the use of ground-based GNSS data and CIT to monitor one consistent picture of both the vertical and horizontal distribution of electron density inhomogeneities in the E region. Therefore, to further expound on the complex subject of E_s morphology, reconstructions from the current technique can complement other E_s observational techniques that might be precise but expensive to run or limited on a spatial and temporal scale. Additionally, the relatively fast computation speed of approximately 7 min on a desktop setting encourages the extension of the developed tomography method into a near real-time 3-D E_s now-cast application for industry that utilize transionospheric radio signals.

6. Conclusion

This paper has presented a novel two-step CIT technique to reconstruct the 3-D maps of daytime sporadic-E based on ground-based GNSS observations. To facilitate the CIT, we have adopted TEC measurements from a dense receiver network, GEONET, located over Japan with more than 1,200 stations. First, on a coarse grid of 1° in the horizontal, 20 km in altitude, and a 15-min assumption of ionosphere stationarity, we reconstruct a more accurate F region structure from a smooth background using the MART algorithm. Then, using the SVD algorithm and a finer grid of 0.4° in the horizontal, 1 km in altitude, and 1.5 min in time, a 3-D E region, 80–180 km in height, is estimated from TEC residues after deducting the F region contribution. To vertically constrain the solution, we use time-dependent EOFs generated from a Chapman model function tuned to manually scaled E_s observations from a network of four ionosondes over Japan. Results from simulation and real observations exhibit that the technique can reconstruct E_s structure with a high degree of fidelity, specifically during strong E_s (*foEs* > 20 MHz). Moreover, 2-D horizontal slices at the height of maximum E_s, corroborate the earlier analyses and expositions on the morphology and dynamics of E_s. That is: E_s shows E-W large elongated frontal structures that can extend several hundred kilometers; the migration is northwestward in the morning and southwestward in the afternoon, with a velocity of 60–100 m/s; the duration of E_s frontal structures can reach tens of minutes to a few hours. The scope of this paper is technically limited to showing that with a correct representation and constraints, a consistent E_s 3-D structure is reproducible from ground-based GNSS data. Specifically of interest from the results is the robustness in tracking the E_s-layer radial-time variation. Such results could be influential and complementary to other E_s observational techniques limited on the space-time scale, thus deepening our understanding of daytime E_s formation and morphology. More so, demonstrated capabilities in future can extend to analyses of the nighttime E region structure and its role during E-F coupling instabilities.

Data Availability Statement

The authors thank the Geospatial Information Authority of Japan (GSI) for GEONET data at https://www.gsi.go.jp/ENGLISH/geonet_english.html, the National Institute of Information and Communications Technology (NICT) for ionosonde data at https://wdc.nict.go.jp/IONO/, the COSMIC Data Analysis and Archive Center (CDAAC) for "ionPrf" data at https://www.cosmic.ucar.edu/, and the World Data Center for Geomagnetism for Dst data at http://wdc.kugi.kyoto-u.ac.jp/dstdir/index.html.

Acknowledgments

This work was supported by JST SPRING Grant Number JPMJSP2110, and partially supported by JSPS KAKENHI Grant Number 21H04518.

References

Aarons, J., & Whitney, H. E. (1968). Ionospheric scintillations at 136 MHz from a synchronous satellite. *Planetary and Space Science*, *16*(1), 21–28. https://doi.org/10.1016/0032-0633(68)90042-1

Andoh, S., Saito, A., & Shinagawa, H. (2021). Temporal evolution of three-dimensional structures of metal ion layer around Japan simulated by a midlatitude ionospheric model. *Journal of Geophysical Research: Space Physics*, *126*(6). https://doi.org/10.1029/2021JA029267

Andoh, S., Saito, A., Shinagawa, H., & Ejiri, M. K. (2020). First simulations of day-to-day variability of mid-latitude sporadic E layer structures. *Earth, Planets and Space*, *72*(1), 1–9. https://doi.org/10.1186/s40623-020-01299-8

Austen, J. R., Franke, S. J., & Liu, C. (1988). Ionospheric imaging using computerized tomography. *Radio Science*, *23*(3), 299–307. https://doi.org/10.1029/RS023i003p00299

Belehaki, A., Jakowski, N., & Reinisch, B. (2004). Plasmaspheric electron content derived from GPS TEC and digisonde ionograms. *Advances in Space Research*, *33*(6), 833–837. https://doi.org/10.1016/j.asr.2003.07.008

Bilitza, D., Altadill, D., Reinisch, B., Galkin, I., Shubin, V., & Truhlik, V. (2016). The international reference ionosphere: Model update 2016. In *EGU general assembly conference abstracts* (pp. EPSC2016–9671).

Bilitza, D., Altadill, D., Truhlik, V., Shubin, V., Galkin, I., Reinisch, B., & Huang, X. (2017). International Reference Ionosphere 2016: From ionospheric climate to real-time weather predictions. *Space Weather*, *15*(2), 418–429. https://doi.org/10.1002/2016SW001593

Das, S. K., & Shukla, A. K. (2011). Two-dimensional ionospheric tomography over the low-latitude Indian region: An intercomparison of ART and MART algorithms. *Radio Science*, *46*(2). https://doi.org/10.1029/2010RS004350

Fan, J., & Ma, G. (2014). Characteristics of GPS positioning error with non-uniform pseudorange error. *GPS Solutions*, *18*(4), 615–623. https://doi.org/10.1007/s10291-013-0359-z

Gołub, G. H., & Van Loan, C. (1989). *Matrix computations*. Johns Hopkins University Press.

Haldoupis, C. (2011). A tutorial review on sporadic E layers. *Aeronomy of the Earth's Atmosphere and Ionosphere*, *2*, 381–394. https://doi.org/10.1007/978-94-007-0326-1_29

Haldoupis, C. (2019). An improved ionosonde-based parameter to assess sporadic E layer intensities: A simple idea and an algorithm. *Journal of Geophysical Research: Space Physics*, *124*(3), 2127–2134. https://doi.org/10.1029/2018JA026441

Haldoupis, C., Meek, C., Christakis, N., Pancheva, D., & Bourdillon, A. (2006). Ionogram height–time–intensity observations of descending sporadic E layers at mid-latitude. *Journal of Atmospheric and Solar-Terrestrial Physics*, *68*(3–5), 539–557. https://doi.org/10.1016/j.jastp.2005.03.020

Hsu, C.-T., Matsuo, T., Yue, X., Fang, T.-W., Fuller-Rowell, T., Ide, K., & Liu, J.-Y. (2018). Assessment of the impact of FORMOSAT-7/COSMIC-2 GNSS RO observations on midlatitude and low-latitude ionosphere specification: Observing system simulation experiments using Ensemble Square Root Filter. *Journal of Geophysical Research: Space Physics*, *123*(3), 2296–2314. https://doi.org/10.1002/2017JA025109

Kelley, M. C. (2009). *The Earth's ionosphere: Plasma physics and electrodynamics*. Academic Press.

Kunitsyn, V. E., & Tereshchenko, E. D. (2003). *Ionospheric tomography*. Springer Science & Business Media. https://doi.org/10.1007/978-3-662-05221-1

Lu, W., Ma, G., & Wan, Q. (2021). A review of voxel-based computerized ionospheric tomography with GNSS ground receivers. *Remote Sensing*, *13*(17), 3432. https://doi.org/10.3390/rs13173432

Ma, G., Gao, W., Li, J., Chen, Y., & Shen, H. (2014). Estimation of GPS instrumental biases from small scale network. *Advances in Space Research*, *54*(5), 871–882. https://doi.org/10.1016/j.asr.2013.01.008

Ma, G., & Maruyama, T. (2003). Derivation of TEC and estimation of instrumental biases from GEONET in Japan. In *Annales geophysicae* (Vol. 21, pp. 2083–2093). https://doi.org/10.5194/angeo-21-2083-2003

Maeda, J., & Heki, K. (2014). Two-dimensional observations of midlatitude sporadic E irregularities with a dense GPS array in Japan. *Radio Science*, *49*(1), 28–35. https://doi.org/10.1002/2013rs005295

Maeda, J., & Heki, K. (2015). Morphology and dynamics of daytime mid-latitude sporadic-E patches revealed by GPS total electron content observations in Japan. *Earth, Planets and Space*, *67*(1), 1–9. https://doi.org/10.1186/s40623-015-0257-4

Maeda, J., Suzuki, T., Furuya, M., & Heki, K. (2016). Imaging the midlatitude sporadic E plasma patches with a coordinated observation of spaceborne InSAR and GPS total electron content. *Geophysical Research Letters*, *43*(4), 1419–1425. https://doi.org/10.1002/2015GL067585

Mao, T., Wang, J., Yang, G., Yu, T., Ping, J., & Suo, Y. (2010). Effects of typhoon Matsa on ionospheric TEC. *Chinese Science Bulletin*, *55*(8), 712–717. https://doi.org/10.1007/s11434-009-0472-0

Mathews, J. (1998). Sporadic E: Current views and recent progress. *Journal of Atmospheric and Solar-Terrestrial Physics*, *60*(4), 413–435. https://doi.org/10.1016/s1364-6826(97)00043-6

Miller, K., & Smith, L. (1975). Horizontal structure of midlatitude sporadic-E layers observed by incoherent scatter radar. *Radio Science*, *10*(3), 271–276. https://doi.org/10.1029/RS010i003p00271

Muafiry, I. N., Heki, K., & Maeda, J. (2018). 3D tomography of midlatitude sporadic-E in Japan from GNSS-TEC data. *Earth, Planets and Space*, *70*(1), 1–12. https://doi.org/10.1186/s40623-018-0815-7

Mungufeni, P., Kim, Y. H., & Ssessenga, N. (2021). Observations of ionospheric irregularities and its correspondence with sporadic E occurrence over South Korea and Japan. *Advances in Space Research*, *67*(7), 2207–2218. https://doi.org/10.1016/j.asr.2021.01.013

Pi, X., Mannucci, A., Lindqwister, U., & Ho, C. (1997). Monitoring of global ionospheric irregularities using the worldwide GPS network. *Geophysical Research Letters*, *24*(18), 2283–2286. https://doi.org/10.1029/97gl02273

Raymund, T. D., Austen, J. R., Franke, S., Liu, C., Klobuchar, J., & Stalker, J. (1990). Application of computerized tomography to the investigation of ionospheric structures. *Radio Science*, *25*(5), 771–789. https://doi.org/10.1029/RS025i005p00771

Razin, M. R. G., & Voosoghi, B. (2016). Regional application of multi-layer artificial neural networks in 3-D ionosphere tomography. *Advances in Space Research*, *58*(3), 339–348. https://doi.org/10.1016/j.asr.2016.04.029

Saito, A., Fukao, S., & Miyazaki, S. (1998). High resolution mapping of TEC perturbations with the GSI GPS network over Japan. *Geophysical Research Letters*, *25*(16), 3079–3082. https://doi.org/10.1029/98GL52361

Saito, S., Suzuki, S., Yamamoto, M., Chen, C.-H., & Saito, A. (2017). Real-time ionosphere monitoring by three-dimensional tomography over Japan. *NAVIGATION, Journal of the Institute of Navigation*, *64*(4), 495–504. https://doi.org/10.1002/navi.213

Saito, S., Yamamoto, M., Hashiguchi, H., & Maegawa, A. (2006). Observation of three-dimensional structures of quasi-periodic echoes associated with mid-latitude sporadic-E layers by MU radar ultra-multi-channel system. *Geophysical Research Letters*, *33*(14). https://doi.org/10.1029/2005GL025526

Šauli, P., & Bourdillon, A. (2008). Height and critical frequency variations of the sporadic-E layer at midlatitudes. *Journal of Atmospheric and Solar-Terrestrial Physics*, *70*(15), 1904–1910. https://doi.org/10.1016/j.jastp.2008.03.016

Shinagawa, H., Miyoshi, Y., Jin, H., & Fujiwara, H. (2017). Global distribution of neutral wind shear associated with sporadic E layers derived from GAIA. *Journal of Geophysical Research: Space Physics*, *122*(4), 4450–4465. https://doi.org/10.1002/2016ja023778

Shubin, V. (2015). Global median model of the F2-layer peak height based on ionospheric radio-occultation and ground-based Digisonde observations. *Advances in Space Research*, *56*(5), 916–928. https://doi.org/10.1016/j.asr.2015.05.029

Shubin, V., Karpachev, A., & Tsybulya, K. (2013). Global model of the F2 layer peak height for low solar activity based on GPS radio-occultation data. *Journal of Atmospheric and Solar-Terrestrial Physics*, *104*, 106–115. https://doi.org/10.1016/j.jastp.2013.08.024

Ssessanga, N. (2018). A tomographic Investigation of mid-latitude nighttime ionospheric E-F coupling. In *42nd COSPAR scientific assembly* (Vol. 42, p. C1.5-7-18).

Ssessanga, N., Kim, Y. H., & Jeong, S.-H. (2017). A statistical study on the F2 layer vertical variation during nighttime medium-scale traveling ionospheric disturbances. *Journal of Geophysical Research: Space Physics*, *122*(3), 3586–3601. https://doi.org/10.1002/2016JA023463

Ssessanga, N., Yamamoto, M., Saito, S., Saito, A., & Nishioka, M. (2021). Complementing regional ground GNSS-STEC computerized ionospheric tomography (CIT) with ionosonde data assimilation. *GPS Solutions*, *25*(3), 1–15. https://doi.org/10.1007/s10291-021-01133-y

Sun, W., Ning, B., Hu, L., Yue, X., Zhao, X., Lan, J., et al. (2020). The evolution of complex E_s observed by multi instruments over low-latitude China. *Journal of Geophysical Research: Space Physics*, *125*(8), e2019JA027656. https://doi.org/10.1029/2019JA027656

Sun, W., Zhao, X., Hu, L., Yang, S., Xie, H., Chang, S., et al. (2021). Morphological characteristics of thousand-kilometer-scale E_s structures over China. *Journal of Geophysical Research: Space Physics*, *126*(2), e2020JA028712. https://doi.org/10.1029/2020JA028712

Sutton, E., & Na, H. (1995). Comparison of geometries for ionospheric tomography. *Radio Science*, *30*(1), 115–125. https://doi.org/10.1029/94RS02314

Tsunoda, R. T., Cosgrove, R. B., & Ogawa, T. (2004). Azimuth-dependent E_s layer instability: A missing link found. *Journal of Geophysical Research: Space Physics*, *109*(A12). https://doi.org/10.1029/2004JA010597

Whitehead, J. (1972). The structure of sporadic E from a radio experiment. *Radio Science*, *7*(3), 355–358. https://doi.org/10.1029/RS007i003p00355

Whitehead, J. (1989). Recent work on mid-latitude and equatorial sporadic-E. *Journal of Atmospheric and Terrestrial Physics*, *51*(5), 401–424. https://doi.org/10.1016/0021-9169(89)90122-0

Wu, D. L., Ao, C. O., Hajj, G. A., de La Torre Juarez, M., & Mannucci, A. J. (2005). Sporadic E morphology from GPS-CHAMP radio occultation. *Journal of Geophysical Research: Space Physics*, *110*(A1). https://doi.org/10.1029/2004JA010701

Xiong, P., Zhai, D., Long, C., Zhou, H., Zhang, X., & Shen, X. (2021). Long short-term memory neural network for ionospheric total electron content forecasting over China. *Space Weather*, *19*(4), e2020SW002706. https://doi.org/10.1029/2020SW002706

Yamamoto, M., Itsuki, T., Kishimoto, T., Tsunoda, R. T., Pfaff, R. F., & Fukao, S. (1998). Comparison of E-region electric fields observed with a sounding rocket and a Doppler radar in the SEEK campaign. *Geophysical Research Letters*, *25*(11), 1773–1776. https://doi.org/10.1029/98gl01055

Yao, Y., Tang, J., Chen, P., Zhang, S., & Chen, J. (2013). An improved iterative algorithm for 3-D ionospheric tomography reconstruction. *IEEE Transactions on Geoscience and Remote Sensing*, *52*(8), 4696–4706. https://doi.org/10.1109/TGRS.2013.2283736

Yizengaw, E., Moldwin, M., Galvan, D., Iijima, B., Komjathy, A., & Mannucci, A. (2008). Global plasmaspheric TEC and its relative contribution to GPS TEC. *Journal of Atmospheric and Solar-Terrestrial Physics*, *70*(11–12), 1541–1548. https://doi.org/10.1016/j.jastp.2008.04.022

Yokoyama, T., Hysell, D. L., Otsuka, Y., & Yamamoto, M. (2009). Three-dimensional simulation of the coupled Perkins and E_s-layer instabilities in the nighttime midlatitude ionosphere. *Journal of Geophysical Research: Space Physics*, *114*(A3). https://doi.org/10.1029/2008JA013789

Yokoyama, T., Yamamoto, M., Fukao, S., Takahashi, T., & Tanaka, M. (2005). Numerical simulation of mid-latitude ionospheric E-region based on SEEK and SEEK-2 observations. In *Annales geophysicae* (Vol. 23, pp. 2377–2384). https://doi.org/10.5194/angeo-23-2377-2005

Zeng, Z., & Sokolovskiy, S. (2010). Effect of sporadic E clouds on GPS radio occultation signals. *Geophysical Research Letters*, *37*(18). https://doi.org/10.1029/2010GL044561